Light Reflections Detection And Correction For Robotic Volumetric PIV

Porcar Galan, L.; Grille Guerra, A.; Sciacchitano, A.; Scarano, F.

DOI
10.55037/lxlaser.21st.59

Publication date
2024

Document Version
Final published version

Published in
Proceedings of the 21st International Symposium on the Application of Laser and Imaging Techniques to Fluid Mechanics

Citation (APA)
Porcar Galan, L., Grille Guerra, A., Sciacchitano, A., & Scarano, F. (2024). Light Reflections Detection And Correction For Robotic Volumetric PIV. In *Proceedings of the 21st International Symposium on the Application of Laser and Imaging Techniques to Fluid Mechanics* Article 59 LISBON Simposia. https://doi.org/10.55037/lxlaser.21st.59

Light reflections detection and correction for Robotic Volumetric PIV

L. Porcar Galan[1], A. Grille Guerra[1,*], A. Sciacchitano[1], F. Scarano[1]

1: Faculty of Aerospace Engineering, Delft University of Technology, Delft, The Netherlands
* Correspondent author: a.grilleguerra@tudelft.nl

Keywords: Particle Image Velocimetry (PIV), PIV processing, reflections, flow diagnostics, image pre-processing

ABSTRACT

Laser light reflection mitigation in Particle Image Velocimetry (PIV) is crucial for accurate flow field measurements. While numerous methods exist for planar PIV, fewer have been developed for volumetric PIV systems, and in particular for coaxial setups like robotic volumetric PIV. Light reflections in volumetric PIV experiments result in high-intensity regions that corrupt particle detection and analysis. This study presents a novel approach for treating light reflections in robotic volumetric PIV experiments. The proposed method uses image filtering and masking techniques in the wavenumber space to separate particle images from reflection regions. The process involves decomposing the image signal into low- and high-wavenumber components using the 2D discrete Fourier transform (DFT) to then use a high-pass filter to attenuate the intensity of the reflection regions. Finally, a step of automated adaptive masking is applied to remove residual reflection areas that the filtering is not able to eliminate. The proposed approach is tested on experimental data obtained from experiments performed using robotic volumetric PIV on two different geometries: a side-view mirror and a rotating two-blade propeller. Comparison between raw and pre-processed images, as well as particle tracking results, is presented. The results from this data comparison show successful removal of reflection-induced artifacts in instantaneous images by using the spatial Fourier filter automated masking approach. The developed image pre-processing strategy effectively removes unsteady light reflection regions in robotic volumetric PIV images, preventing the appearance of spurious particle tracks and improving the accuracy of flow field measurements. The spatial gaps introduced by the masking procedure can be easily filled in via measurements from multiple directions, which are promptly achieved via the robotic volumetric PIV approach.

1. Introduction

Light reflection mitigation in PIV has been a topic of research since the technique was introduced. When the laser light used to illuminate the flow tracers interacts with a solid surface, a significantly higher amount of photons is scattered, reaching the imager and resulting in regions of overwhelmingly high intensity. As a result, these regions of reflection dominate the optical signal of the particle tracers and strongly affect the result of the analysis of the PIV recordings. Mitigation of light reflections can be performed in several ways: when possible, the illumination is sent

tangentially to the surface (Kähler et al., 2006); the solid object surface can be treated with light absorbing paint (Paterna et al., 2013) or using the principle of fluorescence (Depardon et al., 2005). Many studies have identified approaches employing image processing. Popular choices exploit the differences in the time scales of particles (fast and small) compared to those of reflections (slow and big), by subtracting the minimum or mean pixel intensity over a temporal sequence of images or spatial subdomain bigger than the particle image respectively (Adrian & Westerweel, 2011). Methods based on frequency (high-pass) filter have also proven successful for stationary or slowly-moving reflections (Sciacchitano & Scarano, 2014) or interfaces (Theunissen et al., 2008). More recently, image filtering based on POD has been proposed (Mendez et al., 2017). Finally, a method that isolates the particle images from the reflections in planar PIV has been proposed by Adatrao & Sciacchitano (2019), where the spatial characteristics of the reflection (anisotropy) is exploited.

Comparatively, the treatment of reflections for 3D PIV experiments and in particular for coaxial systems (Schneiders et al., 2018) has barely been discussed in the literature and most recipes are based on the best practice gained from planar PIV. In volumetric PIV experiments, light reflections are more diffuse as a result of the distributed illumination. Due to the high-intensity of reflection regions, particle detection algorithms tend to produce abundant false positives (ghost particles, Elsinga et al., 2006) and corrupt the cross-correlation (for tomo-PIV) or particle tracking (for PTV approaches) analyses. The domain affected by these reflections emanates from the reflection propagating along the line of sight of the camera with the reflection in view. While most of the existing strategies for the mitigation of reflections in planar PIV are also helpful for volumetric PIV, the specific features of illumination and imaging for 3D systems suggest revising the procedure. The spatial properties of the reflection region are a first factor for consideration, together with the multiplicity (sometimes redundancy) of views, typical of 3D PIV systems.

For robotic volumetric PIV (Jux et al., 2018), the coaxial arrangement of laser illumination and imagers (Schneiders et al., 2018) typically causes the appearance of glare regions when a curved object is illuminated (Jux et al., 2020). The ghost particles produce in turn a large number of spurious particle tracks after the Shake-the-Box analysis (Schanz et al., 2016), corrupting the velocity statistics along an extended region approximately aligned along the optical axis of the system. When dealing with unsteady reflections (e.g. due to a moving object), pre-processing based on filters in the time or frequency domains is not effective and specific solutions need to be sought for.

The present work approaches the above problem from the space-wavenumber domains with filtering and masking techniques that make use of the analysis of the image in the wavenumber space. The working principle of image filtering in the wavenumber space is presented and

exemplified. Furthermore, the same analysis is considered for use in adaptive image masking. Wind tunnel experiments are conducted to verify the validity of the principle for robotic volumetric PIV measurements, both for stationary and moving objects. Evaluation of pre-processed recordings from single views of the robotic PIV system using particle tracking demonstrates the effectiveness of the technique in removing spurious trajectories. To compensate for the data gaps produced by the filtering/masking procedure, redundant robot views are required, as commonly employed with robotic volumetric PIV for full-domain coverage.

2. Working principle

Robotic volumetric PIV systems tend to produce large reflection regions that are imaged over extended portions of the image and with variable intensity. This phenomenon results from the conical illumination. Its reflection remains approximately conical on flat surfaces, or it can diverge, or even converge on curved surfaces. In many circumstances, the reflected light reaches back the imagers causing a large, diffused region of high intensity. In the worst case, the latter can saturate the detector. In many other cases, the reflection exceeds the intensity of the tracers. Figure 1 represents schematically the situations mentioned above for a generic coaxial volumetric velocimeter (CVV).

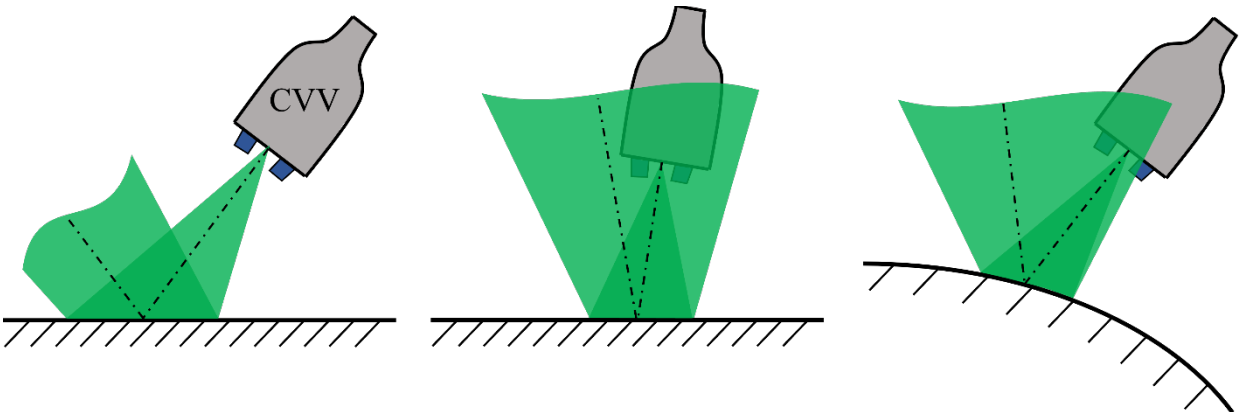

Figure. 1 Schematic description of coaxial system and intercepted object. The illumination beam may not reach the imagers for strongly oblique configuration (left). For quasi-normal condition (middle) or when the object is convex (right), the beam reflects back along the imaging views.

Although unwanted, the pattern of light reflected from the object strongly differs from the light of the individual tracers. The former covers a wide region, while the latter appear as a Gaussian dot of approximately 3 pixels (when considering diffraction dominated imaging).

4.1.Image-wavenumber space filtering

The scale separation of the optical signal from particles and reflection is at the basis of the present method. In analogy to the temporal high-pass filter (Sciacchitano & Scarano, 2014), whereby the pixel intensity signal is decomposed into a low-frequency (object reflection) and high-frequency component (transiting particle image), the image signal is decomposed here into low- and high-wavenumber components making use of the 2D discrete Fourier transform (DFT).

The digital image of pixel coordinates $\boldsymbol{I}(x,y)$ is represented in the wavenumber space $\boldsymbol{J}(k_x, k_y)$ by computing its DFT. The latter operation is performed using the fast Fourier transform (FFT) algorithm. This transformation can be rearranged such that the DC component appears in the centre of the image, with the axes spanning from the negative Nyquist wavenumber (-0.5 1/px) to the positive one (0.5 1/px). The *duality* principle between space and wavenumber determines the corresponding properties of $\boldsymbol{J}$ from given image properties. In particular, the Fourier transform of a small dot in the physical image results into a broad (and relatively low) intensity distribution in the wavenumbers space. Comparatively, the broad region of reflection appearing in the image, once Fourier transformed, produces a relatively high-intensity sharp peak in the origin of the wavenumber space.

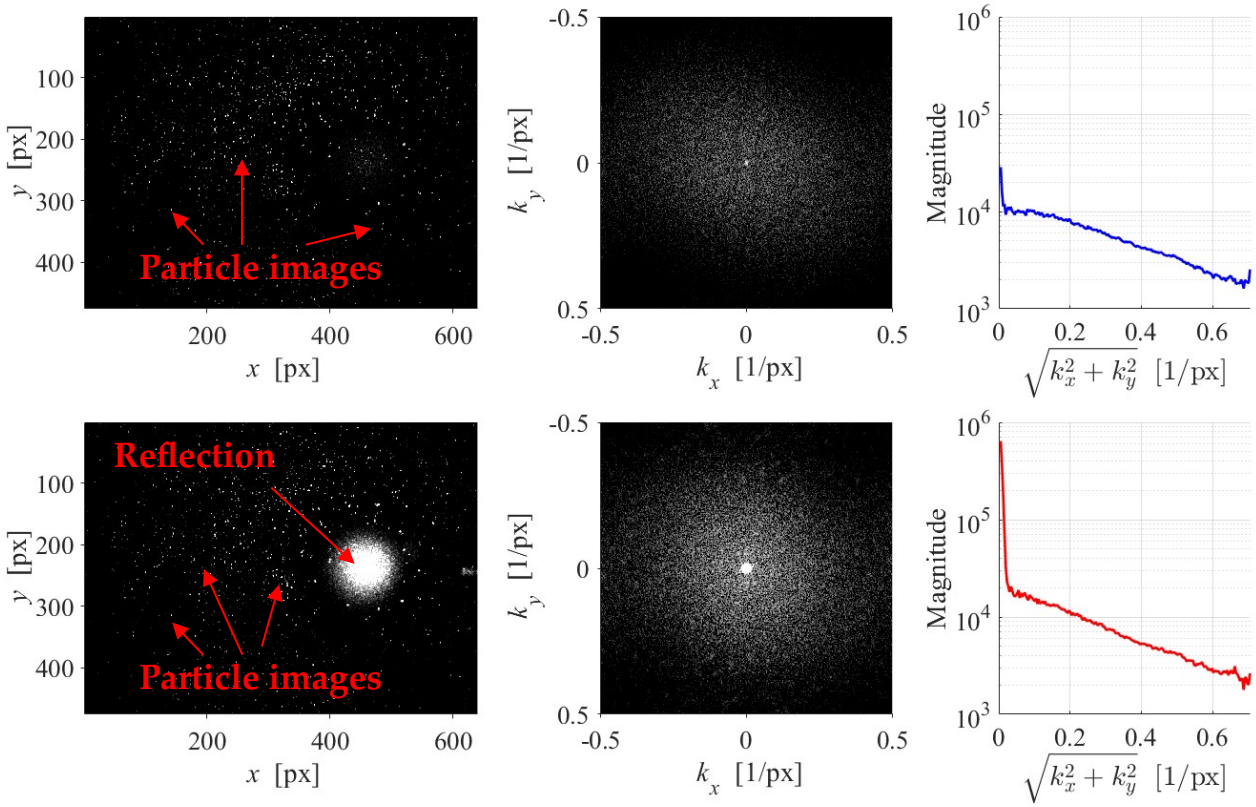

Figure. 2 Example of instantaneous particle image in the physical space (left), the magnitude of its Fourier transform (middle), and the magnitude averaged over the azimuth (right), for an image without (top) and with (bottom) the presence of a light reflection.

The following example makes use of real images acquired with robotic PIV around a sphere (for further details, check Jux et al. (2020)). Figure 2 (top) illustrates the typical image obtained in absence of light reflections, together with the corresponding magnitude of $\boldsymbol{J}(k_x,k_y)$. The intensity distribution in the wavenumber space features a broad distribution with a grainy pattern. The latter is due to the random distribution of particles, and can be homogenised by averaging over an ensemble of images or simply by transforming to a polar coordinate system and averaging over the azimuth, as shown in Figure 2 (right). A small peak at the origin (DC) is noticed in the figure, which is due to the pixel intensity being semi-definite positive, yielding a nonzero image mean value. At the bottom row of Figure 2, an image affected by the object reflection is shown, along its Fourier transform. The reflection has a diameter of approximately 130 px, and the Fourier transform exhibits a peak decaying at the corresponding wavenumber ($k_{refl} = 1/130 = 0.007\,1/\mathrm{px}$). In conclusion, the image intensity in the wavenumber space can be considered as the superposition of two distinct contributions, which can be separated on the basis of their different wavelength.

The intensity of the light reflection region can be reduced via a high-pass filter. The filter shape is chosen as a Gaussian weighting function of standard deviation σ, as shown in Equation (1) and Figure 3. The cut-on wavenumber ($k_{cuton} \equiv \sigma$) should be chosen corresponding to that of the reflection region. Multiplying the transformed image with the high-pass version of the filter kernel, a filtered version of the original image is obtained via the inverse FFT algorithm.

$$H\left(k_x, k_y\right) = 1 - e^{-\frac{k_x^2}{2k_{cuton}^2}} \cdot e^{-\frac{k_y^2}{2k_{cuton}^2}} \tag{1}$$

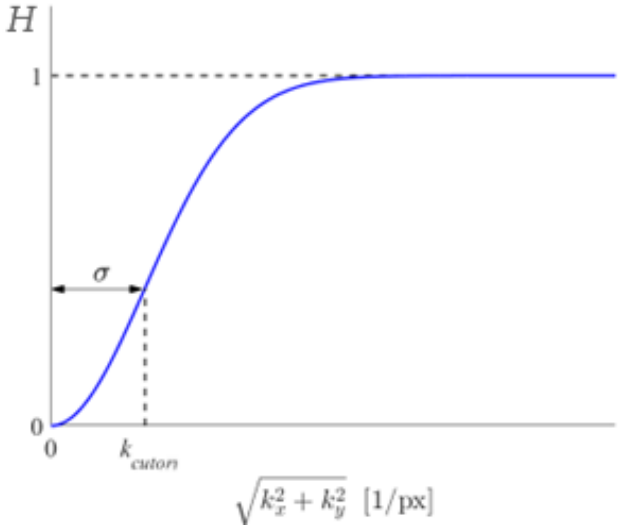

Figure. 3 High pass Gaussian kernel in the wavenumber space. The standard deviation of the Gaussian distribution, σ, represents the cut-on wavenumber k_{cuton}.

As illustrated in Figure 4, this filtering strategy attenuates the intensity of the reflected object image compared to that of the particle tracers. However, the choice of k_{cuton} may result in the reflections not being fully eliminated ($k_{cuton} \ll k_{refl}$) or the particle images being attenuated and distorted by the filter ($k_{cuton} \gg k_{refl}$). Besides, light reflections in experimental images do not follow exactly a Gaussian distribution and often contain certain level of granularity or speckle (represented by smaller wavelengths) due to surface imperfections and laser coherence.

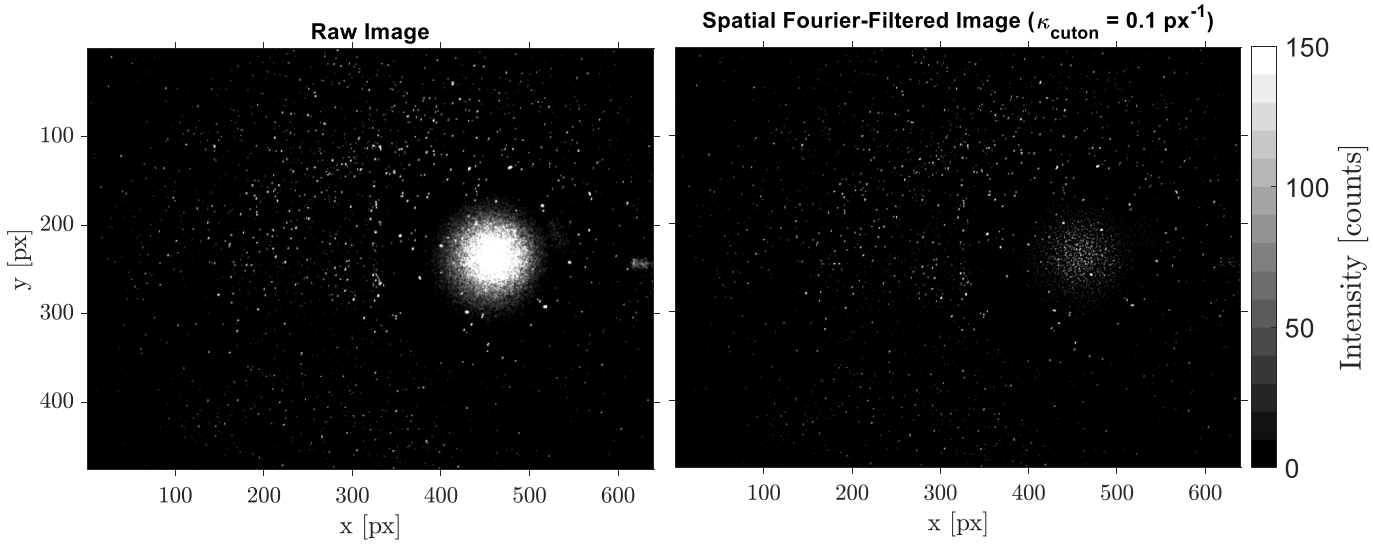

Figure. 4 (Left) Raw image and (right) Pre-processed image with spatial Fourier filter ($k_{cuton} = 0.1\ px^{-1}$)

4.2.Reflection mask generation

The procedure to filter out the reflection can be made less sensitive to the choice of k_{cuton} if the filter is not used directly as a weighting function, but rather to guide an operation of automated masking. The high-pass filter is known to affect the intensity of the object reflection more than that of the tracer particles. A comparison between the original and filtered images will highlight the reflection areas. This comparison is made using the structural similarity index (*SSIM*, Wang et al., 2004), which takes into account changes not only in intensity but also in contrast and structure. The *SSIM* comparison between images i and j takes the form:

$$SSIM(i,j) = \frac{(2\mu_i\mu_j + C_1)(2\sigma_{ij} + C_2)}{(\mu_i^2 + \mu_j^2 + C_1)(\sigma_i^2 + \sigma_j^2 + C_2)}, \quad (2)$$

where μ_i, μ_j, σ_i, σ_j and σ_{ij} are the local (over a Gaussian window) mean, standard deviation and covariance of the images. C_1 and C_2 are small regularization constants. The *SSIM* calculation provides a normalized comparison between images, with low values corresponding to areas affected by reflections. In the low-value regions, there are also a few particles that are being picked up. These particles have suffered a decrease in their intensity after the spatial Fourier filtering,

hence this is why they appear as low SSIM value regions in the SSIM map, as shown in Figure 5 (left). However, the reflection regions clearly show two main characteristics: low SSIM value and large area. Therefore, to mask out these regions from the filtered image, two conditions must be applied on the SSIM map: first, a threshold on the SSIM value to keep only the regions that have changed most; then, a threshold on the area of the remaining blobs to retain only the largest ones, corresponding to reflections. This allows to generate the mask of the reflection regions presented in Figure 5 (right).

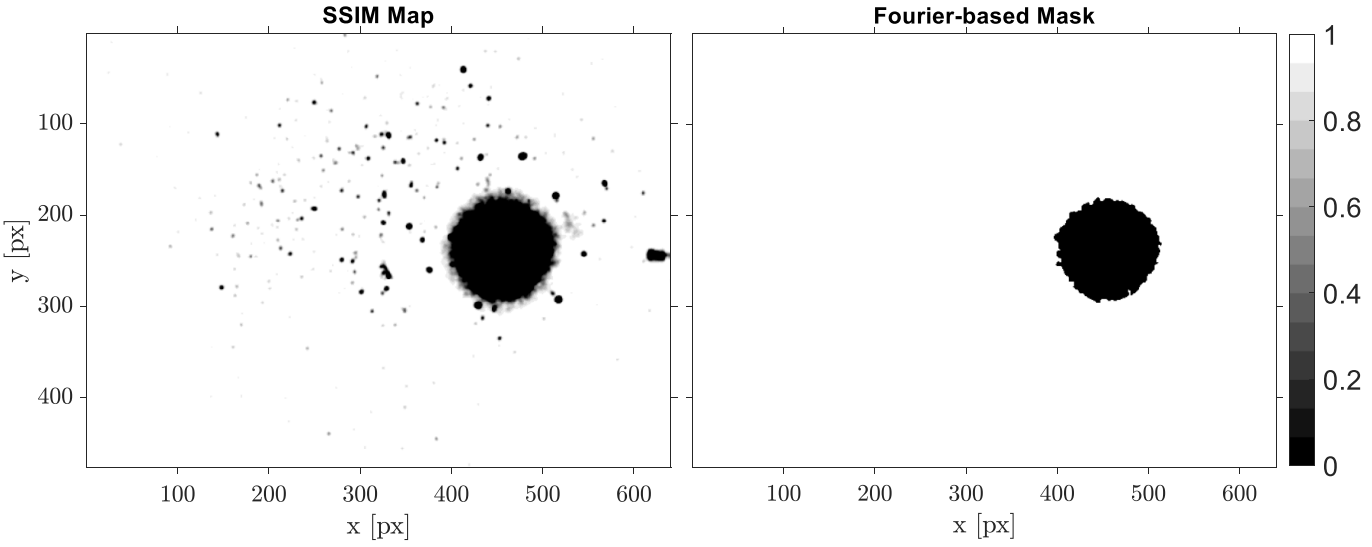

Figure. 5 (Left) SSIM map and (right) Generated mask from SSIM map.

This mask is then applied to the filtered image to eliminate the reflection content. As a last step, an intensity normalization on the entire set of images is performed with the aim to achieve a uniform intensity distribution across the image. The masked image is presented next to the original raw image in Figure 6 (top row). The masked image has null intensity in the reflection region, preventing any particle to be detected along that line of sight of the velocimeter. The corresponding particle tracks, coloured by velocity magnitude, are shown in Figure 6 (bottom). This result is void of spurious trajectories (false positives), but also of valid ones (false negatives), confirming that the image pre-processing approach is effective in eliminating the effect of light reflections and the associated spurious tracks, which are difficult to eliminate in the 3D processing stage. The dataset is however voided in the propagated masked region, which introduces the problem of spatial gaps. The latter is to be accounted for by multiple independent views from directions not affected by object reflection, contributing to filling the gaps - partly or completely.

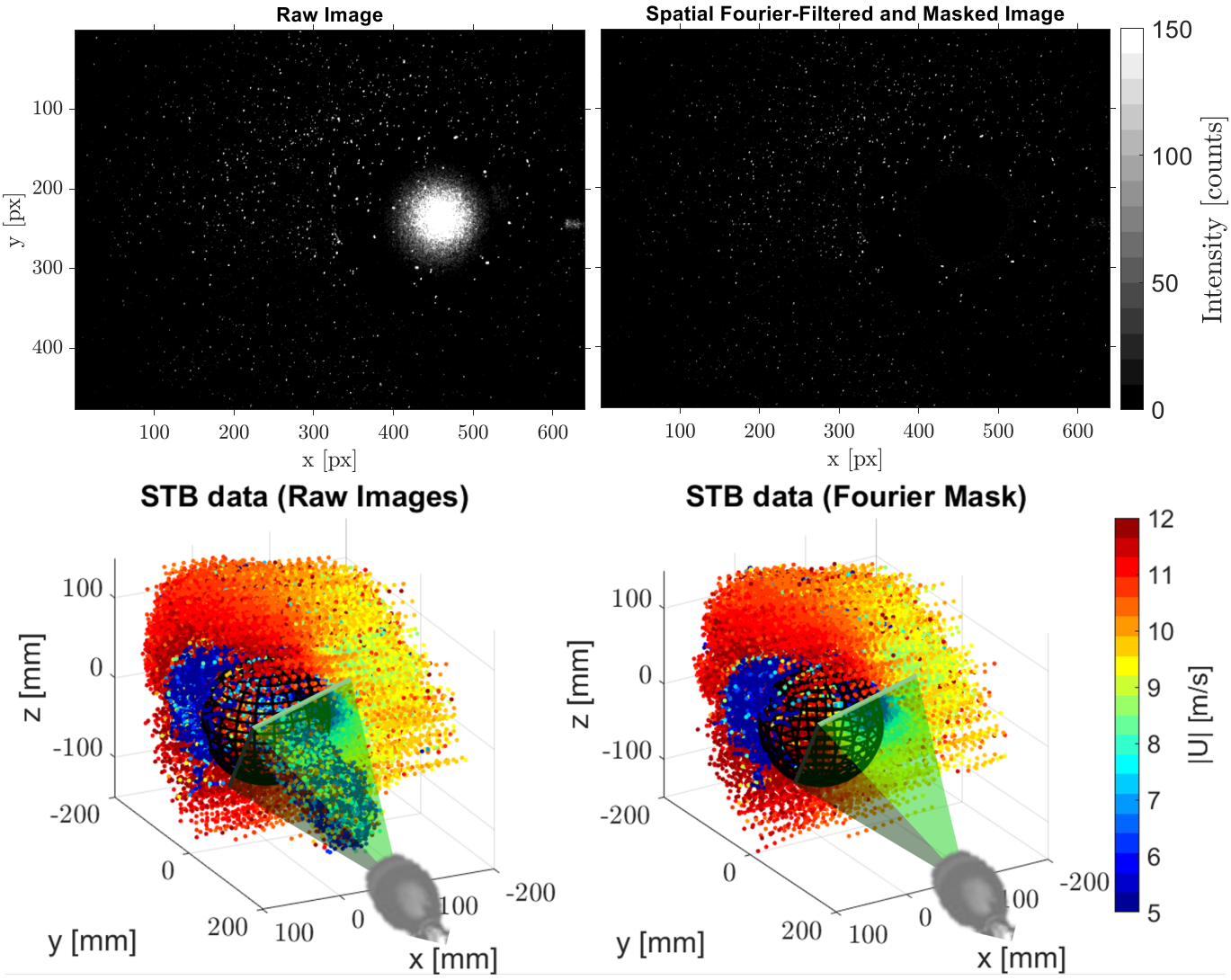

Figure. 6 Top: (Left) Raw image and (right) Pre-processed image with spatial Fourier filter ($k_{cuton} = 0.1\ px^{-1}$); bottom: corresponding Shake-the-Box results.

3. Experimental assessment

To evaluate the proposed image pre-processing approach, two different experimental datasets have been considered, featuring a side-view mirror with dimensions 5cmx10cmx15cm (for further details, refer to Saredi et al., 2021), and an APC propeller 7x5 with 2 blades and constant pitch with a diameter of 7 inch/17.7 cm (Cueto Corral, 2023) installed in pusher configuration. Experiments using robotic volumetric PIV are conducted in the W-tunnel (0.6 x 0.6 m^2 test section) in the Flow Physics and Technology Laboratories of TU Delft. The free stream velocity is set at 15 m/s for the side-view mirror and 7 m/s for the propeller, with a rotational speed of the latter of 3600 RPM. The flow is seeded with sub-millimetre neutrally-buoyant helium-filled soap bubbles (HFSB, Scarano et al., 2015) released by an array comprising 204 generators (Saiz et al., 2022). The robotic

volumetric PIV system consists of a LaVision *Minishaker Aero* CVV manipulated with a Universal Robots *UR5* arm. The velocimeter comprises four 10-bit CMOS imagers in diamond arrangement, set at a resolution of 640 × 476 pixels and operated at a rate of 821 Hz. A Quantronix *Darwin-Duo* Nd-YLF laser (2 × 25 mJ at 1 kHz) is used as illumination source, delivered at the centre of the velocimeter through an integrated optical fiber. The measurement volume, whose shape is best described by a truncated pyramid, extends 40 cm in depth, spanning 12 × 16 cm^2 at its top end and up to 36 × 48 cm^2 at its base. The experimental arrangements are shown in Figure 7.

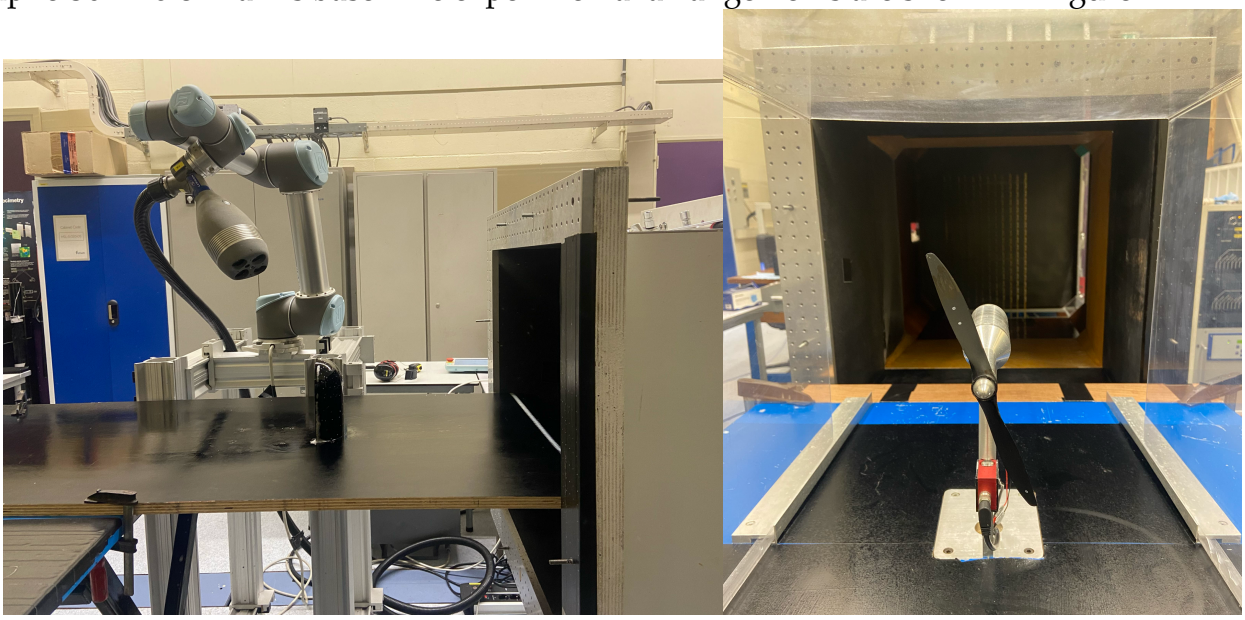

Figure. 7 Experimental setups for the side-view mirror (left) and propeller (right) flow experiments.

The side-view mirror's robot sequence consisted of 8 robot positions with 5,000 images each, recorded with Double-Frame Shake-the-Box (DF-STB) with the aid of a velocity predictor (Saredi et al., 2020) adopting the following two time steps: $dt_1 = 100\ \mu s$ and $dt_2 = 500\ \mu s$. Regarding the propeller, 9 measurement volumes with 5,000 images each are recorded in Time-Resolved Shake-the-Box (TR-STB) mode.

Test number	Model	Velocity [m/s]	Acquisition mode	Images acquired	Number of views
1	Side-view mirror	15	DF-STB	5,000 ($dt_1 = 100\ \mu s$) 5,000 ($dt_2 = 500\ \mu s$)	8
2	Propeller	7	TR-STB	5,000	9

Table. 1 Summary of the experimental campaign parameters.

The raw images are pre-processed with the state-of-the-art Butterworth time filter (with a filter length of 9 images) for reference, and also the proposed spatial Fourier filtering and masking approach with a cut-on wavenumber $\kappa_f = 0.1\ px^{-1}$. Then, the obtained images are processed with the particle tracking algorithm Shake-the-Box.

The data obtained from Shake-the-Box shows the velocity of particles tracked over time as scattered data over the measurement domain. In order to simplify and to facilitate interpretation of the flow field, a binning step is performed to transform the unstructured velocity information to a structured one. The measurement volumes acquired for the side-view mirror are averaged in space and time within sphere-shaped regions (or bins) of 15 mm diameter with a 75% overlap of neighboring bins, yielding a spacing of 3.75 mm between velocity vectors. For the propeller, the data is interrogated within spherical bins with a diameter of 23.6 mm and 75% overlap, resulting in 6 mm of space between velocity vectors. Following Agüera et al. (2016), a quadratic (2nd order) weighting function is employed on all cases to perform the velocity averaging inside each bin. Additionally, the set of measurement volumes are merged into a single dataset and the binning with the same parameters as for the individual views is applied.

4. Results

4.1.Side-view mirror test case

A set of four consecutive recordings from a single view acquired on the side-view mirror are presented in Figure 8 (advancing from left to right), as obtained with three different image pre-processing strategies (from top to bottom rows): no pre-processing applied (raw images), Butterworth time filter and spatial Fourier filter and mask. These show the presence of large foam blobs caused by occasional malfunctioning of a few bubble generators, which pose a challenge to particle tracking, as their appearance is random and can blind particles being tracked.

As illustrated by this example, the proposed method is highly effective at removing steady reflections from the test object's surface, comparatively to the Butterworth filter. As these foam blobs appear and disappear at a similar rate of the particle tracks, the Butterworth time filter is unable to eliminate them. However, the spatial Fourier filtering and masking method is able to identify these regions in each instantaneous image and, then eliminate them by masking. The masking generates a void in the image that will appear in the 3D data. This empty spaces in the image can be filled in thanks to the multiple-view capability of robotic volumetric PIV. By measuring views that overlap, regions that are blank in one view can contain data in another view, thus making it possible to fill in the gaps when merging all the measurement volumes.

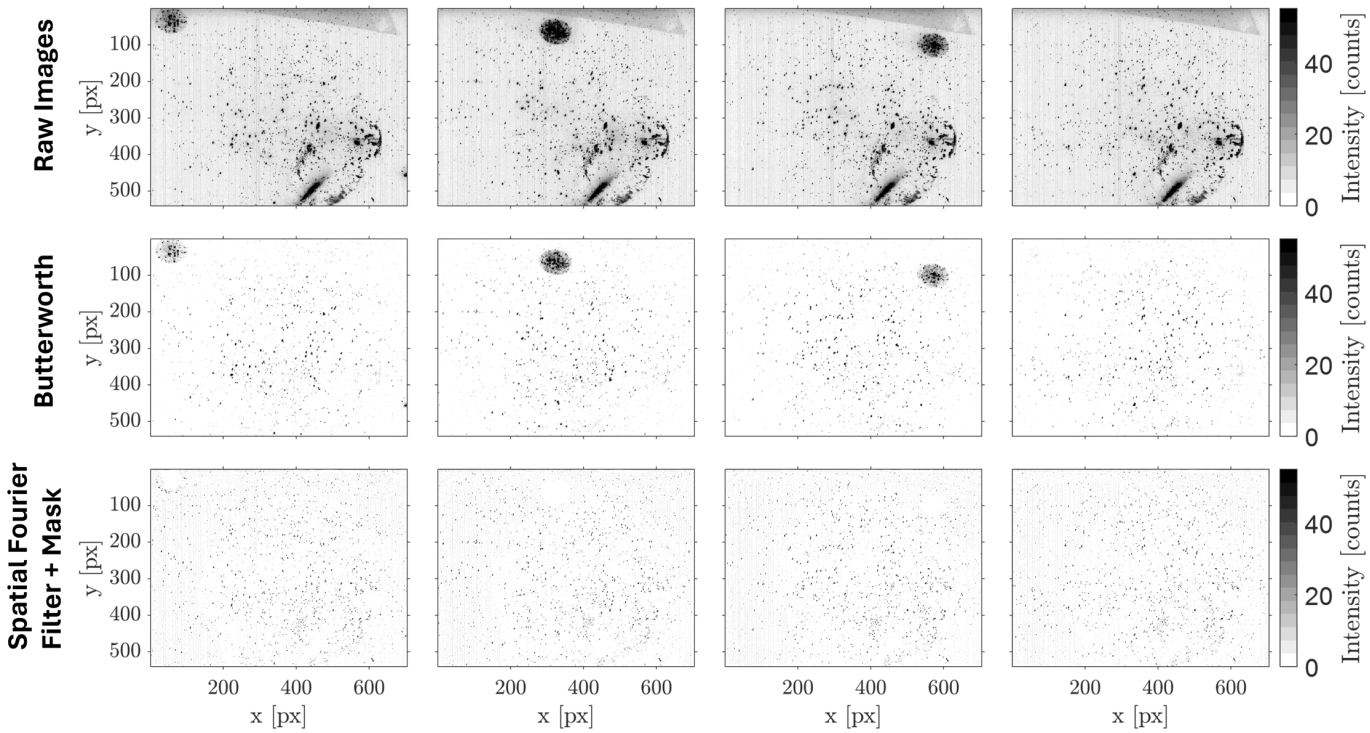

Figure. 8 Set of consecutive raw and pre-processed images with Butterworth time filter and Spatial Fourier Filter + Mask of the side-view mirror.

The results of processing the images with STB are presented in Figures 9 and 11, by showing the binned velocity field on XZ and YZ planes, respectively. The results are given for three single views as well as the merged dataset. For the latter, the standard deviation of the velocity magnitude is also given in the figure. Overall, the resulting velocity field of the masked case does resemble the Butterworth filter's one, with a similar mean velocity in the single views and in the merged case, with almost no blank spaces appearing in the single views (they are filled in thanks to the amount of data after processing 5,000 images). The Butterworth case shows a small region of outliers at the front of the side-view mirror in View 4 (see Figure 9). This is due to foam attached to the surface of the mirror that the time filter is not able to fully remove because of its fluctuating behavior as illustrated in Figure 10. Conversely, the spatial Fourier filter and mask approach is able to completely remove this region, avoiding its appearance in the processed results.

The blank space in the 2D images is translated into an empty gap in the velocity field along the line of sight of the velocimeter (see Figure 11, View 4). However, this void is almost entirely filled in the merged dataset velocity field, thanks to the presence of other views that contain information within this region of the domain. In this case, View 8 is an example of measurement volume that has data where there View 4 presents a gap (top left of the mirror).

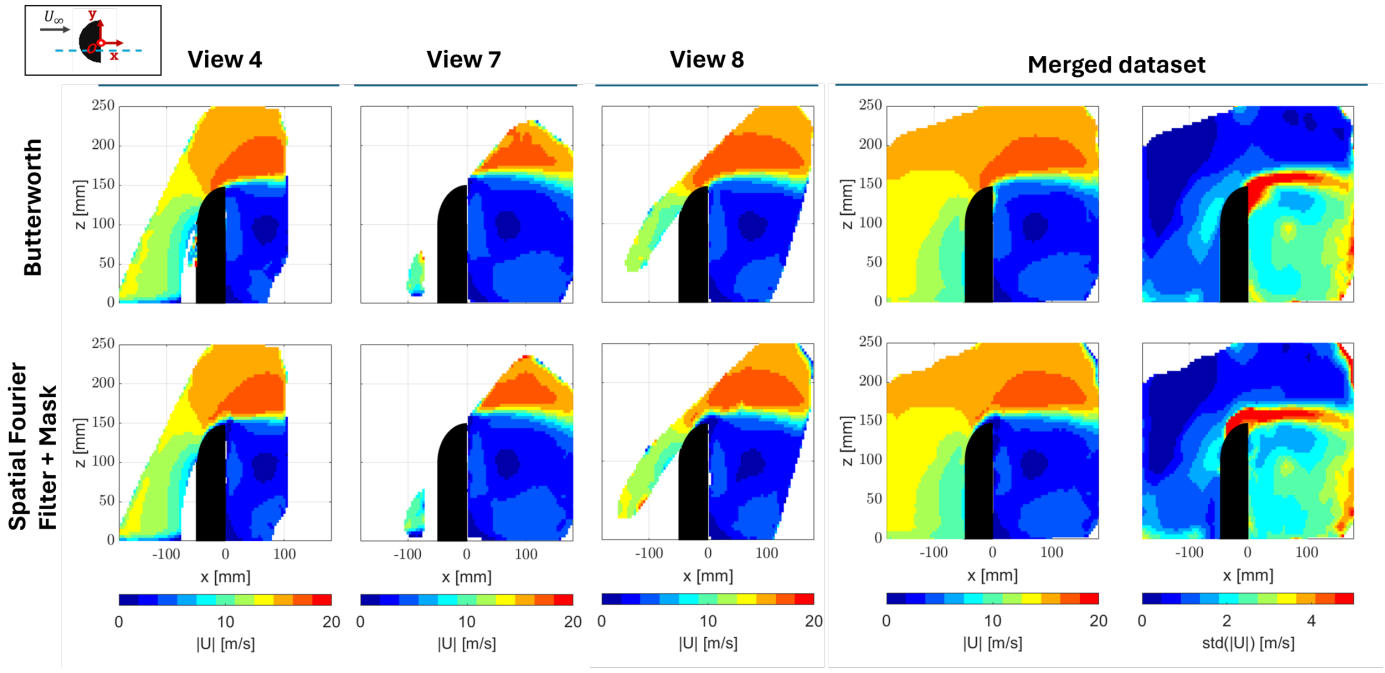

Figure. 9 $|U|$ and std($|U|$) on XZ plane at y = 0 mm for single views and merged dataset.

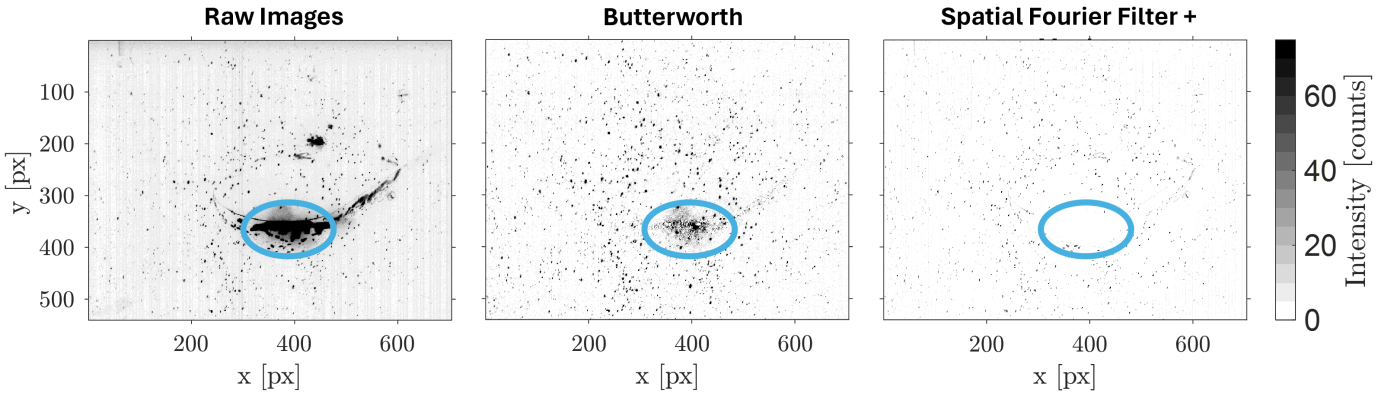

Figure. 10 Instantaneous raw and pre-processed images of unsteady reflection on side-view mirror's surface.

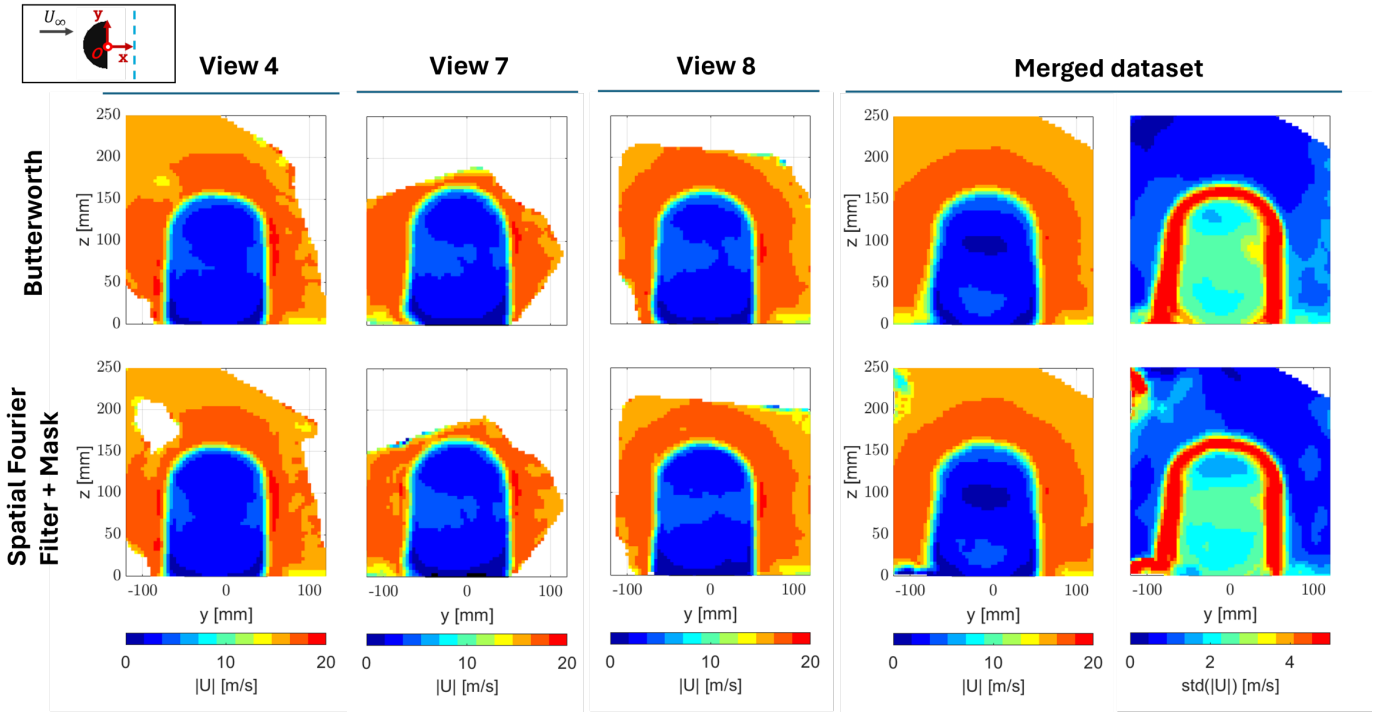

Figure. 11 |U| and std(|U|) on YZ plane at x = 30 mm for single views and merged dataset.

Comparing the merged datasets of both methods, the mean velocity is in excellent agreement, but the standard deviation presents slightly different features, particularly in the shear layer in Figure 9. The Butterworth filter result shows high standard deviation in the near wake of the mirror, while the masking method exhibits high standard deviation on top-left of the mirror. These phenomena are due to the local effect from the presence of residual reflections not being fully removed. Despite this, the proposed spatial Fourier filtering and masking method performs as well as the Butterworth time filter in the case of stationary objects.

4.2.Propeller test case

In the case of the propeller, there are three main sources of reflections: steady reflections from the vertical strut, unsteady reflections from the vibration of the horizontal strut and hub, and unsteady reflections from the rotating blades. Being it steady, the reflection on the vertical strut can be easily removed via the application of the Butterworth filter. However, this technique fails to remove the other reflections that are fluctuating over time. This is exemplified in Figure 12, where a set of four consecutive recordings are shown for the case of raw images, pre-processed Butterworth time-filtered and spatial Fourier filter and mask images.

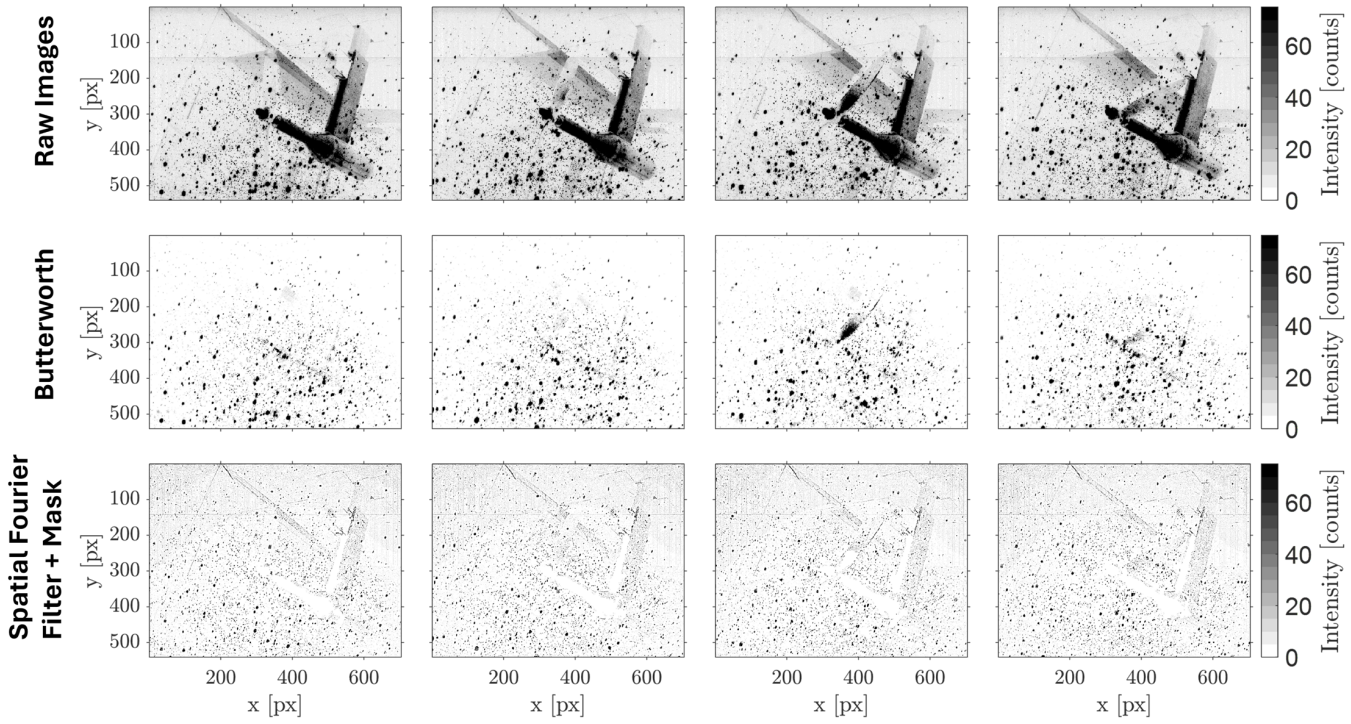

Figure. 12 Set of consecutive raw and pre-processed images with Butterworth time filter and Spatial Fourier Filter + Mask of the propeller.

The reflections are easily identified and occupy a significant region of the image. The Butterworth filter is able to eliminate the reflection on the vertical struts, but it fails to mitigate the high intensity regions corresponding to reflections on the moving objects. With the spatial Fourier filtering and masking approach, all the spurious regions are successfully and entirely removed from each instantaneous recording. Notice that the shape of the mask changes for each recording, allowing a robustly elimination of all reflections that the Butterworth filter could not remove. This results in a reflection-free set of images that will avoid the presence of spurious tracks in the processed Shake-the-Box data.

Figure 13 shows the resulting velocity field on the YZ plane for two single views and the merged-view case, showing the wake flow field 5 cm downstream of the propeller. The Butterworth filter attenuates the reflection, but does not eliminate it completely. In fact, despite the application of the Butterworth filter, residual artifacts from the propeller blades are still visible (as shown in Figure 12), whose intensities propagate along the line-of-sight of the velocimeter when processing with the Shake-the-Box algorithm. The spatial Fourier filter and mask velocity field presents regions that are not captured in the single views compared to the Butterworth filter's result, in particular, at the bottom of the propeller's slipstream in View 1, and bottom and top-right in View 2. However, as expected, these gaps are successfully filled in when merging all the views together. The flow in the entire propeller's slipstream can be evaluated in both cases, exhibiting a velocity increase from

7 m/s to 8 m/s. The additional masking step allows to successfully remove the reflection from the blades, thus resulting in a more accurate evaluation of the flow field. This is visible in the mean flow, where spurious high-velocity regions on top of the propeller's slipstream, present in the Butterworth filter's result, are removed when using the Fourier filter and masking, but even more evidently in the fluctuations root-mean-square contour, where the Butterworth's filter result largely overestimates the fluctuations due to the presence of spurious tracks.

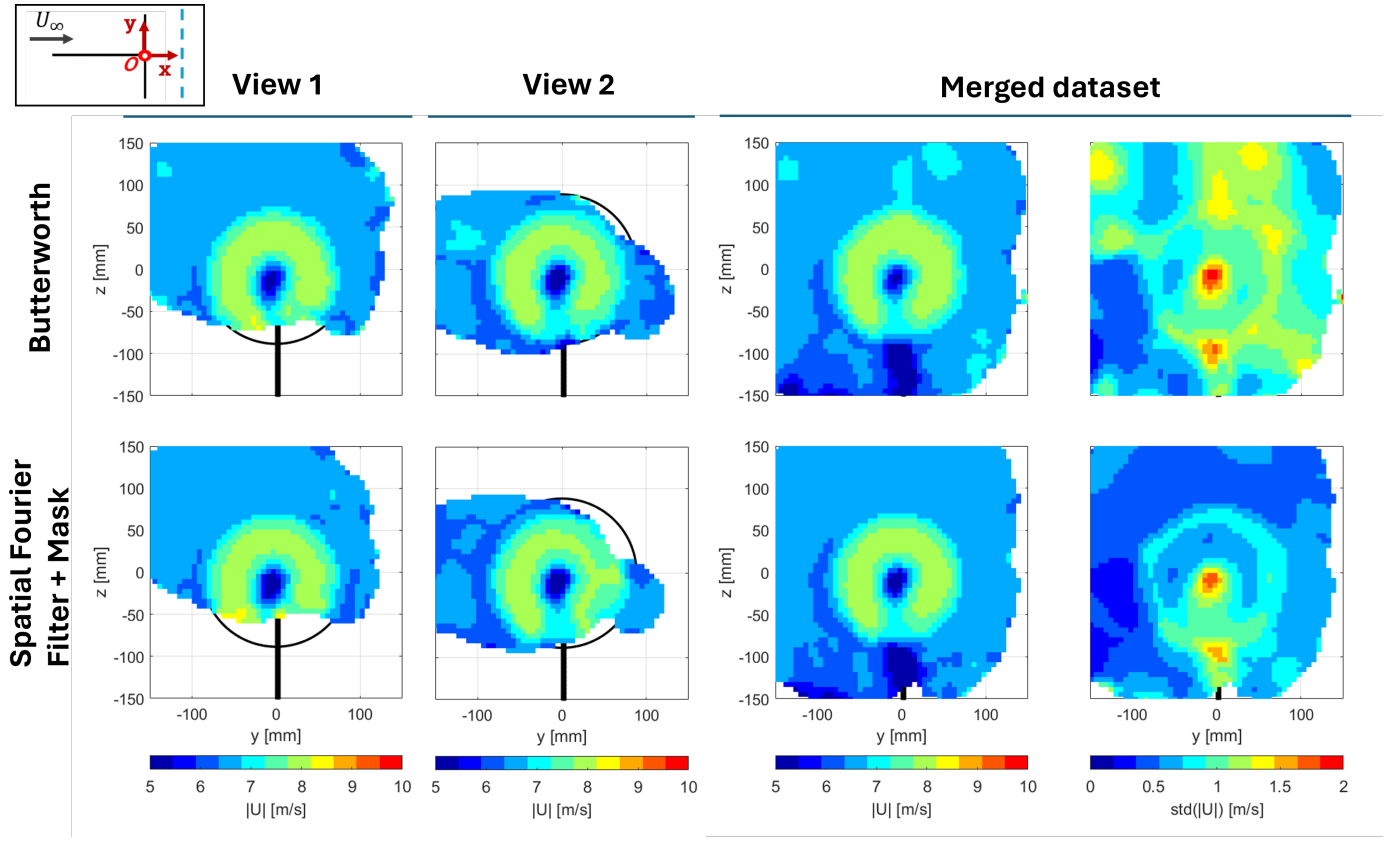

Figure. 13 |U| and std(|U|) on YZ plane at x = 50 mm for single views and merged dataset.

The XY plane at the propeller's streamtube symmetry plane is presented in Figure 14 for two single views and the merged dataset. This plane shows a top view of the wake from the propeller's slipstream. The Butterworth flow field shows the influence of the propeller horizontal strut reflection, which appears as a high mean velocity region as observed in View 4. This does not occur for the masking method, which shows a small gap, consequence of masking this area. Since View 2 contains data in the region within this void, the latter is entirely filled in the merged-view case. For the complete velocity field, the mean velocity and its standard deviation is shown. It is important to highlight that the spatial Fourier filtering and masking approach has a significantly lower standard deviation compared to the Butterworth, indicating much more reliable results. This is thanks to the successful removal of both steady and unsteady reflections with the masking

approach. Conversely, the Butterworth shows a significant high standard deviation in the region of the horizontal strut as a result of the reflection that emanates from this part of the geometry.

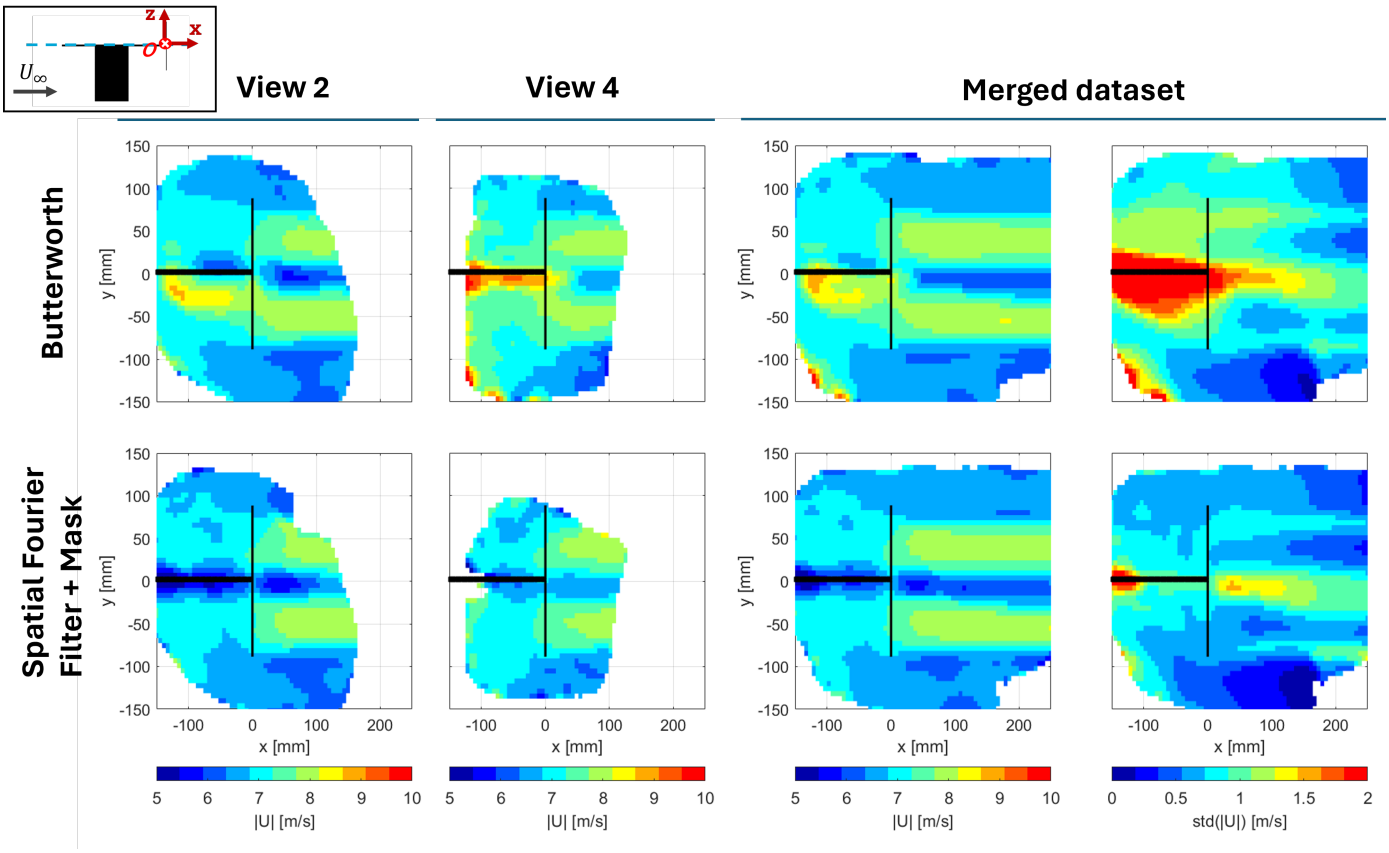

Figure. 14 |U| and std(|U|) on XY plane at z = 0 mm for single views and merged dataset.

5. Conclusions

This study introduced and evaluated a novel approach for mitigating laser light reflections in instantaneous data from Robotic Particle Image Velocimetry (PIV) experiments. This method aimed to address the challenge of high-intensity reflection regions corrupting particle detection and analysis in volumetric PIV systems, particularly in Robotic PIV. The process involved image filtering and masking techniques in the wavenumber space, by using the 2D discrete Fourier transform (DFT) to decompose the image signal into low- and high-wavenumber components. A high-pass filter is applied to attenuate the intensity of reflection regions composed mainly by low-wavenumber content; then, an additional automated adaptive masking step is implemented to remove residual reflection areas that the filtering could not eliminate. The proposed methodology is tested and compared to a state-of-the-art technique on experimental data obtained from robotic volumetric PIV experiments on the flow around two different geometries: a side-view mirror and a propeller. Comparison between raw and pre-processed images, as well as particle tracking results, confirmed the successful removal of reflection-induced artifacts using the spatial Fourier filter automated masking approach.

The steady reflections from the side-view mirror case are properly masked, yielding a velocity field similar to the Butterworth's. Both Butterworth and proposed approach are successful at removing all spurious regions, showing a similar mean velocity and standard deviation fields. However, there are some regions of unsteady reflections from foam attached to the mirror's surface that the Butterworth fails to fully remove, which results in outliers in the corresponding velocity field. This does not occur for the masking method, which successfully removes all the regions of reflections, either steady or unsteady.

The propeller test case was chosen to assess the effectiveness of the proposed method in presence of unsteady reflections in individual instantaneous images. Most of the propeller's measurement volumes showed a big steady reflection coming from the strut and support, and moving reflections from the rotating blades. Also, the horizontal strut suffered a slight vibration due to the blades' rotation, which posed an additional challenge for the state-of-the-art technique. The Butterworth time filter could remove the steady reflections from the support, but failed to eliminate the unsteady regions. Instead, the spatial Fourier filtering and masking approach could mask all existing reflections, both steady and unsteady, in each instantaneous acquired image, thus mitigating their contributions to the 3D Shake-the-Box results. Furthermore, a set of consecutive images for different views have been displayed proving the method's capability to generate an adaptive mask for each of the instantaneous images, adopting the shape of the spurious regions and effectively capturing and removing the reflection on the rotating blade. This capability of masking reflection regions results in a velocity field free of spurious tracks, thus yielding much more accurate turbulence statistics. In the masked regions, clearly no particle images are visible, thus resulting in spatial gaps in the 3D velocity field. Nonetheless, it has been shown that the spatial gaps can be easily filled in when using robotic volumetric PIV and performing the flow measurements from different viewing directions.

References

Adatrao, S., & Sciacchitano, A. (2019). Elimination of unsteady background reflections in PIV images by anisotropic diffusion. *Measurement Science and Technology*, *30*(3). https://doi.org/10.1088/1361-6501/aafca9

Adrian, R. J., & Westerweel, J. (2011). Particle Image Velocimetry. Cambridge University Press. https://books.google.nl/books?id=jbDl2-yHbooC

Agüera, N., Cafiero, G., Astarita, T., & Discetti, S. (2016). Ensemble 3D PTV for high resolution turbulent statistics. *Measurement Science and Technology*, 27(12), 124011. doi:10.1088/0957-0233/27/12/124011

Cueto Corral, P. (2023). Propeller Slipstream Characterisation by Large-Scale PIV: An experimental study for Isolated Propeller and Propeller-Wing Interaction [Master's Thesis, Delft University of Technology]. http://resolver.tudelft.nl/uuid:6d071306-faef-4cb9-9c21-a184fc8aaf0e

Depardon, S., Lasserre, J. J., Boueilh, J. C., Brizzi, L. E., & Borée, J. (2005). Skin friction pattern analysis using near-wall PIV. *Experiments in Fluids*, *39*(5), 805–818. https://doi.org/10.1007/s00348-005-0014-8

Elsinga, G. E., Van Oudheusden, B. W., & Scarano, F. (2006). Experimental assessment of Tomographic-PIV accuracy. *13th Int Symp on Applications of Laser Techniques to Fluid Mechanics Lisbon, Portugal, 26-29 June, 2006*, *1993*, 26–29.

Jux, C., Sciacchitano, A., & Scarano, F. (2020). Flow pressure evaluation on generic surfaces by robotic volumetric PTV. *Measurement Science and Technology*, *31*(10). https://doi.org/10.1088/1361-6501/ab8f46

Jux, C., Sciacchitano, A., Schneiders, J. F. G., & Scarano, F. (2018). Robotic volumetric PIV of a full-scale cyclist. *Experiments in Fluids*, *59*(4), 1–15. https://doi.org/10.1007/s00348-018-2524-1

Kähler, C. J., Scholz, U., & Ortmanns, J. (2006). Wall-shear-stress and near-wall turbulence measurements up to single pixel resolution by means of long-distance micro-PIV. *Experiments in Fluids*, *41*(2), 327–341. https://doi.org/10.1007/s00348-006-0167-0

Mendez, M. A., Raiola, M., Masullo, A., Discetti, S., Ianiro, A., Theunissen, R., & Buchlin, J. M. (2017). POD-based background removal for particle image velocimetry. *Experimental Thermal and Fluid Science*, *80*, 181–192. https://doi.org/10.1016/j.expthermflusci.2016.08.021

Paterna, E., Moonen, P., Dorer, V., & Carmeliet, J. (2013). Mitigation of surface reflection in PIV measurements. *Measurement Science and Technology*, *24*(5). https://doi.org/10.1088/0957-0233/24/5/057003

Saiz, G. G., Sciacchitano, A., & Scarano, F. (2022). On the closure of Collar's triangle by optical diagnostics. *Experiments in Fluids*, *63*(8), 128. https://doi.org/10.1007/s00348-022-03468-9

Saredi, E., Sciacchitano, A., & Scarano, F. (2020). Multi-Δt 3D-PTV based on Reynolds decomposition. Measurement Science and Technology, 31(8), 084005.

Saredi, E., Tumuluru Ramesh, N., Sciacchitano, A., & Scarano, F. (2021). State Observer data assimilation for RANS with time-averaged 3D-PIV data. Computers & Fluids, 218, Article 104827. https://doi.org/10.1016/j.compfluid.2020.104827

Saredi, E., Sciacchitano, A., & Scarano, F. (2022). Outlier detection for PIV statistics based on turbulence transport. *Experiments in Fluids*, *63*(1), 1–10. https://doi.org/10.1007/s00348-021-03368-4

Scarano, F., Ghaemi, S., Caridi, G. C. A., Bosbach, J., Dierksheide, U., & Sciacchitano, A. (2015). On the use of helium-filled soap bubbles for large-scale tomographic PIV in wind tunnel experiments. *Experiments in Fluids*, *56*(2). https://doi.org/10.1007/s00348-015-1909-7

Schanz, D., Gesemann, S., & Schröder, A. (2016). Shake-The-Box: Lagrangian particle tracking at high particle image densities. *Experiments in Fluids*, *57*(5), 1–27. https://doi.org/10.1007/s00348-016-2157-1

Schneiders, J. F. G., Scarano, F., Jux, C., & Sciacchitano, A. (2018). Coaxial volumetric velocimetry. *Measurement Science and Technology*, *29*(6), 065201. https://doi.org/10.1088/1361-6501/aab07d

Sciacchitano, A., & Scarano, F. (2014). Elimination of PIV light reflections via a temporal high pass filter. *Measurement Science and Technology*, *25*(8), 084009. https://doi.org/10.1088/0957-0233/25/8/084009

Theunissen, R., Scarano, F., & Riethmuller, M. L. (2008). On improvement of PIV image interrogation near stationary interfaces. *Experiments in Fluids*, *45*(4), 557–572. https://doi.org/10.1007/s00348-008-0481-9

Wang, Z., Bovik, A. C., Sheikh, H. R., & Simoncelli, E. P. (2004). Image Quality Assessment: From Error Visibility to Structural Similarity. *IEEE Transactions on Image Processing*, *13*(4), 600–612. https://doi.org/10.1109/TIP.2003.819861